

# Post-Buckling Mechanics of a Square Slender Steel Plate in Pure Shear

MARIA E. MOREYRA GARLOCK, SPENCER E. QUIEL, PETER Y. WANG,  
JOSÉ ALÓS-MOYA and JONATHAN D. GLASSMAN

---

## ABSTRACT

Thin (slender) steel plates possess shear strength beyond the elastic buckling load, which is commonly referred to as the post-buckling capacity. Semi-empirical equations based on experimental tests of plate girders have been used for decades to predict the ultimate post-buckling strength of slender webs. However, several recent studies have shown that the current models for predicting the ultimate shear post-buckling capacity of thin plates are based on some incorrect assumptions regarding their mechanical behavior. As a result, the current design equations provide an approximate estimate of capacity for the range of parameters in the test data upon which they are founded. This paper explores the fundamental behavior of thin plates under pure shear. Such a fundamental examination of shear post-buckling behavior in thin plates is needed to enable design procedures that can optimize a plate's shear strength and load-deformation performance for a wider range of loading and design parameters. Using finite element analyses, which are validated against available results of previous experimental tests, outputs such as plastic strains, von Mises stresses, principal stresses, and principal stress directions are examined on a buckled plate acting in pure shear. The internal bending, shear, and membrane stresses in the plate's finite elements are also evaluated. In this study, these evaluations are performed for a simply supported plate with an aspect ratio equal to 1.0 and slenderness ratio equal to 134. Results show that localized bending in the plates due to the out-of-plane post-buckling deformations appear to be a significant factor in the ultimate shear post-buckling capacity of the plate. Also, the compressive stresses continue to increase beyond the onset of elastic buckling in some regions of the plate, contrary to current design assumptions. Overall, this study provides new insights into the mechanics of shear post-buckling behavior of thin plates that can be exploited for design procedures that are consistent with mechanical behavior.

**Keywords:** shear, buckling, tension field, slender plates, web, plate girder.

---

## INTRODUCTION

Deep steel beams (i.e., plate girders) have thin webs and are commonly used in steel construction for buildings but most notably in bridges. The design of these elements is often controlled by the shear strength of the slender web plate. Web plates that elastically buckle due to shear load still possess a significant amount of post-buckling shear strength. Post-buckling capacity is utilized in the design of many bridge girders due to high web slenderness, which is necessitated by large girder depths and weight/material

savings. This post-buckling behavior has attracted the attention of researchers and engineers since the 1880s (e.g., Basler, 1961; Wagner, 1931; Wilson, 1886). Since 1931, more than a dozen proposals have been developed to explain and predict the post-buckling shear strength of thin webs in plate girders (e.g., Höglund, 1997; Porter et al., 1975). A detailed discussion of the differences between several of the aforementioned proposals is provided by White and Barker (2008). Despite these numerous proposals, the true mechanics and post-buckling behavior are still not fully understood, particularly the contributions of the compression field and vertical stiffeners to the ultimate post-buckling shear strength.

Previous publications have provided extensive discussions on the various proposed plate shear buckling models throughout the literature (Ziemian, 2010; White and Barker, 2008; Yoo and Lee, 2006), and all the models are based on tension field action. Tension field theory posits that the main source of this post-buckling shear strength is the development of tensile stresses in a defined diagonal field, which is mobilized after the onset of elastic shear buckling. Recent research, however, has shown that the fundamental assumptions upon which tension field action is based do not represent the full mechanical response of web shear buckling (Yoo and Lee, 2006; Glassman and Garlock, 2016; Jha, 2016).

---

Maria E. Moreyra Garlock, Associate Professor, Princeton University, Princeton, NJ. Email: mgarlock@princeton.edu (corresponding)

Spencer E. Quiel, Assistant Professor, Lehigh University, Bethlehem, PA. Email: seq213@lehigh.edu

Peter Y. Wang, Graduate Student, Princeton University, Princeton, NJ. Email: pywang@princeton.edu

José Alós-Moya, Ph.D., P.E., Researcher/Production Manager, UPV/ACCIONA, València, Spain. Email: joalmo11@upv.es

Jonathan D. Glassman, Ph.D., P.E., Senior Engineer, Exponent Inc., Los Angeles, CA. Email: glassman.jonathan@gmail.com

---

Paper No. 2017-22R

In addition, the current AISC *Specification* (2016) recognizes that the vertical stiffener does not carry the full vertical component of the tension field force. In previous editions, this stiffener was designed for an area consistent with the assumed vertical component of the tension field force, whereas it is currently designed for flexural stiffness only. This change rightly recognizes that the vertical stiffener provides lateral stiffness to define the web panelization—it does not act as an anchor for the tension field. As noted in the AISC *Specification* Commentary: “...transverse stiffeners in I-girders designed for shear post-buckling strength, including tension field action, are loaded predominantly in bending due to the restraint they provide to lateral deflection of the web. Generally, there is evidence of some axial compression in the transverse stiffeners due to the tension field, but even in the most slender web plates permitted by the AISC *Specification*, the effect of the axial compression transmitted from the post-buckled web plate is typically minor compared to the lateral loading effect. Therefore, the transverse stiffener area requirement from prior AISC *Specifications* is no longer specified” (AISC, 2016). However, the design equations that predict the post-buckling capacity are still based on the original tension field design procedures. Using the current approach, the load path for the tension field action is, therefore, incomplete—the vertical component of the diagonal tension field must be resolved via a different mechanism. The study presented in this paper provides, for the first time, insights to the behavior of thin web plates that, with more investigation, can lead to updated design recommendations that include a completed load path.

This paper explores the fundamental behavior of thin plates under pure shear. Using validated finite element analyses, outputs such as plastic strains, von Mises stresses, principal stresses, and principal stress directions are examined on the buckled plate. The through-thickness bending and membrane stresses in the plate elements are also evaluated. These evaluations are performed for a plate with an aspect ratio equal to 1.0 and slenderness ratio equal to 134. Examining this single case provides novel insights into plate

shear buckling behavior that will be used as a basis for future work, which will examine a wider range of plate parameters.

### FINITE ELEMENT MODEL

The plate used for this study is based on standard plans for typical steel girder highway bridges specified by the Federal Highway Administration (FHWA, 1982). A 90-ft (27.4-m) span design was used as a prototype, where the depth,  $D$ , equals 58 in. (1473 mm) and the web thickness,  $t_w$ , equals  $\frac{7}{16}$  in. (11 mm). In practice, many of these girders are designed with a transverse stiffener spacing,  $a$ , greater than  $D$ ; however, in this study we assume  $a = D$ . Future work will examine other stiffener spacings. The steel was modeled with a yield stress equal to 50 ksi (345 MPa), a modulus of elasticity equal to 29,000 ksi (200 GPa), and Poisson’s ratio equal to 0.3. It will be shown that the steel remained in the elastoplastic region for the range of strains encountered in the analyses (well before strain-hardening occurs).

The finite element (FE) model was developed in the software Abaqus (Dassault Systemes, 2011) using the simply supported boundary conditions shown in Figure 1. Note that the boundary conditions used here represent an approximation of the actual boundary conditions and may incorporate flanges and stiffeners, each of varying stiffness. To achieve perfectly symmetric stress results, the boundary conditions used by the authors differ only slightly from those used by Glassman and Garlock (2016), which restrained the  $Y$ -translation on the left side instead of applying a load. The elastic critical shear buckling load,  $V_{cr}$ , and the ultimate post-buckling shear load,  $V_u$ , are not affected by this slight modification in boundary condition.

Yoo and Lee (2006) used boundary conditions that were different from both configurations mentioned earlier. In their studies, the  $z$ -direction translation is free on all four sides. Such a boundary condition represents a lower-bound solution for  $V_u$ . The current study’s boundary conditions assume axially rigid flanges and are thus closer to an upper-bound solution. All boundary conditions discussed here result in

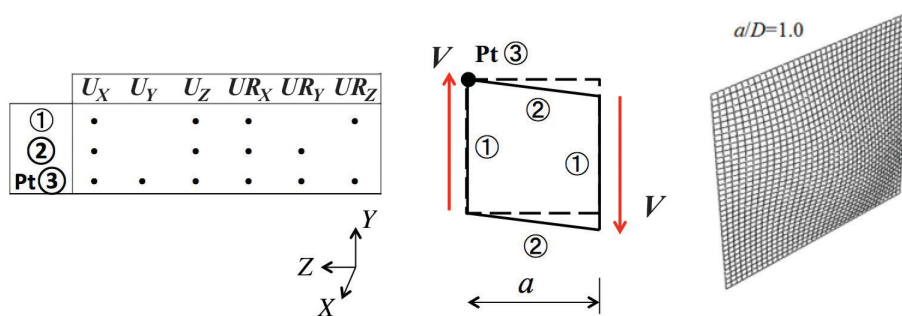


Fig. 1. Boundary conditions of the FE model (left), and mesh density in first mode buckled shape (right). Location 3 is a point (Pt) on the upper left corner.

the same  $V_{cr}$ . Comparing  $V_u$  using the Yoo and Lee (2006) boundary conditions to that produced by the current study's boundary conditions (Figure 1), one obtains  $V_u$  values equal to 437 kips and 593 kips, respectively, when analyzing the prototype plate. The current study's results match those of Glassman and Garlock (2016), which correlated well to experimental results (as will be discussed later in this paper). The authors, therefore, proceed with the boundary conditions of Figure 1 for the remainder of this paper.

The thin plate was meshed using S4 shell elements (doubly curved, general-purpose, finite membrane strains) with four integration points on the surface, as shown in Figure 2. A preliminary study was conducted to determine an appropriate number of section points through the depth, in which three, five, seven, and nine section points at each surface integration point were evaluated by examining stress values and shear load sustained at  $V = V_u$ . The results for five, seven, and nine section points differed by less than 1%, and five section points as shown in Figure 2 are therefore used for all other analyses discussed in this paper.

To capture the plate transition from its initial unbuckled state to post-buckling behavior to ultimate shear strength, nonlinear analyses were conducted using a modified Riks procedure. These analyses require the insertion of an initial geometric imperfection to perturb the mesh prior to loading, which allows the load-displacement curve to proceed beyond the buckling bifurcation point and progress into the post-buckled behavior until  $V_u$  is reached (Glassman and Garlock, 2016). To create this initial geometric imperfection, the eigenmode shape associated with the lowest elastic positive eigenvalue is multiplied by a defined scale factor. Previous research by Garlock and Glassman (2014) found that a scale factor of  $D/10,000$  was sufficient for these models, and this scale factor was therefore selected for the present study. Mesh convergence studies were conducted using an eigenvalue extraction analysis. The final mesh selected is

shown in Figure 1 and is equal to  $37 \times 37$  elements [approximately 1.57 in. (40 mm) square each].

Using this approach, the FE solution for the elastic shear buckling load,  $V_{cr}$ , equaled 345 kips (1535 kN). This value has less than 1% error compared to a theoretical solution of 343 kips (1526 kN), which is obtained from Equation 1:

$$\tau_{cr} = k \frac{\pi^2 E}{12(1-\nu^2) \left( \frac{D}{t_w} \right)^2} \quad (1)$$

In Equation 1,  $\tau_{cr}$  is the elastic shear buckling stress,  $E$  is Young's modulus,  $\nu$  is Poisson's ratio,  $D$  is the depth of the plate,  $t_w$  is the plate thickness, and  $k$  is the elastic shear buckling coefficient. The value of  $k$  is a function of the span-to-depth (aspect) ratio ( $a/D$ ) of the plate and the boundary conditions applied to its edges (Timoshenko and Gere, 1961). For a plate with  $a/D = 1$  and simply supported on all four edges,  $k = 9.34$ .  $D/t_w$  is the slenderness ratio, which is a measure of how susceptible the plate girder is to web shear buckling. The elastic critical shear buckling load,  $V_{cr}$ , is calculated by multiplying Equation 1 by  $D \times t_w$ .

The modeling approach described earlier has also been validated via comparison to experimental test data for various  $a/D$  and  $D/t_w$  ratios. Glassman and Garlock (2016) considered the results of 16 previous experiments whose results are published in Basler et al. (1960), Bergfelt and Hovik (1968), Kamtekar et al. (1972), Rockey and Skaloud (1972), Evans et al. (1977), and Narayanan and Rockey (1981). Glassman and Garlock's (2016) FE models used the same setup conditions as discussed earlier and showed very close agreement with the ultimate post-buckling shear capacity,  $V_u$ , of each plate. Specifically, the FE models predicted  $V_u$  values to within ~10% of the published experimental values with one exception where the flange-to-web thickness ratio ( $t_f/t_w$ ) was quite large compared to other tests (thus influencing that plate's boundary conditions more so than the other validation cases).

## RESULTS

### Sign Conventions and Definitions

To properly interpret the finite elements results, the definitions and sign conventions of the stresses, moments and rotations are defined in this paper as follows, in the context of the Abaqus output:

- Tensile stresses are positive and compressive stresses are negative.
- SP:1 and SP:5 refer to the section points on the two surfaces of the plate as shown in Figure 2.
- The element stresses,  $\sigma_1$ ,  $\sigma_2$  and  $\sigma_{12}$  are defined in Figure 3(a) in the positive direction.

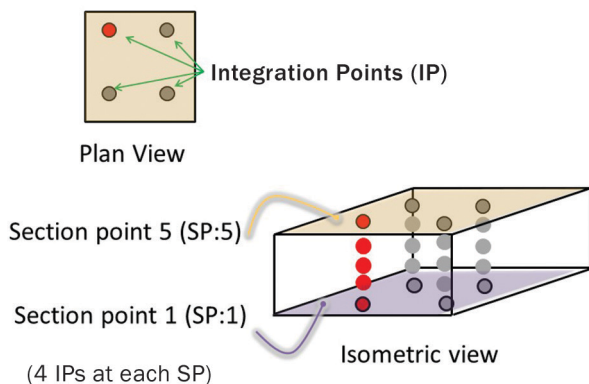


Fig. 2. Integration points and section points on each shell finite element.

- Maximum principal stresses ( $\sigma_{max}$ ) are the maximum positive value, thus typically corresponding to maximum tensile stresses. If no tension is present, the value will be negative, thus corresponding to the minimum compressive value [see Figure 3(b)].
- Minimum principal stresses ( $\sigma_{min}$ ) are the maximum negative value, thus typically corresponding to maximum compressive stresses. If no compression is present, the value will be positive, thus corresponding to the minimum tensile value [see Figure 3(b)].
- Von Mises stresses are defined for the principal plane stress condition defined by Equation 2, where  $\sigma_y$  is the yield stress. Figure 4 plots this yield surface.

$$\sigma_y^2 = \sigma_{max}^2 + \sigma_{min}^2 - \sigma_{max}\sigma_{min} \quad (2)$$

Figure 5 shows the shear force-deformation plot with  $V_{cr}$  and  $V_u$  for this plate labeled for clarity. Deformation is measured at the lower right corner of the plate as shown by the dot in the inset figure. Note that the plot can be divided into three phases of shear loading. Phase I represents the elastic state prior to buckling. In phase II, the plate has exceeded  $V_{cr}$  but still exhibits nearly linear behavior. In phase III, the plate's force-deformation behavior becomes highly nonlinear. For this plate, the boundary between phases II and III lies approximately at the shear halfway between  $V_{cr}$  and  $V_u$ . In the following sections, the stresses and strains throughout the plate will be evaluated at two values of loading: (1) in phase II at  $V = 1.15 \times V_{cr}$  (when the plate has recently buckled) and (2) in phase III at  $V_u$  (when the plate has reached its peak shear load during post-buckling response).

### Ultimate Shear Post-Buckling Load, $V_u$ , and Deformation

Figure 6 illustrates the final deformed shape at the ultimate (post-buckling) shear load,  $V_u$ , that, for this plate, equals 593 kips (2636 kN). The out-of-plane deformations are manifested in three half-wavelengths or bulges from point B to point D. The surface shown in Figure 6 represents the SP:5 face from Figure 2. Therefore, along the “tension field” (from

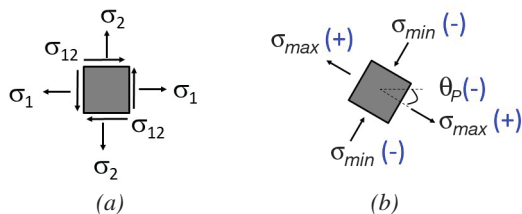


Fig. 3. (a) Positive stresses on element; (b) principal stresses and principal stress direction (with Abaqus sign convention in parentheses).

point A to point C, where the red color represents maximum out-of-plane positive displacement), it will be shown that the SP:5 stresses will be in tension and SP:1 stresses will be in compression due to the significant bending in the plate. Conversely, in Figure 6, where the dark blue color shows large negative displacement, SP:5 stresses will be in compression and SP:1 stresses will be in tension. A thorough analysis of the stresses will be discussed in sections to follow, where it will be shown that the plate bending due to this post-buckling out-of-plane deformation dominates the response when  $V_u$  is reached.

### Plate Behavior Just after Elastic Buckling

Before the plate reached the elastic shear buckling load  $V_{cr}$ , the FE results were consistent with the theoretical behavior of a plate under pure shear: The angle of the principal stress,  $\theta_p$ , was  $45^\circ$ , and the principal stresses in tension and compression ( $\sigma_{max}$  and  $\sigma_{min}$ , respectively) were equal and opposite to one another and also equal to the shear stress [ $V/(D \times t_w)$ , where  $V$  is the applied load]. Note that Abaqus does not output  $\theta_p$ —this value was derived using  $\sigma_1$ ,  $\sigma_2$  and  $\sigma_{12}$  with the well-established equation based on Mohr's circle. In this section, the state of the plate when the shear  $V = 1.15 \times V_{cr}$  (i.e., near the beginning of post-buckling behavior) is examined to enable a comparison to ultimate post-buckling behavior when  $V_u$  is reached. The following behavior is observed:

- *Principal stress direction,  $\theta_p$* : Figure 7 plots the  $\theta_p$  contours for  $V/V_{cr} = 1.15$ . It can be seen that this angle has not changed significantly from the pre-buckling state when this angle was  $45^\circ$ .

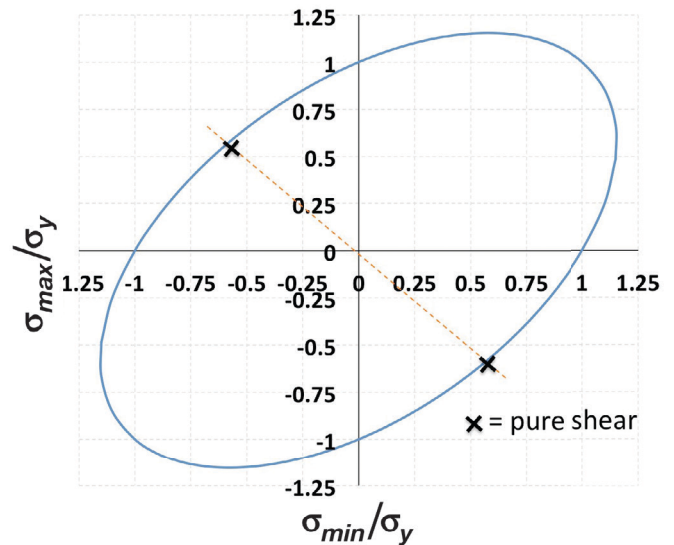


Fig. 4. Von Mises yield surface.

- *Principal stresses:* Figure 8 plots the  $\sigma_{min}$  and  $\sigma_{max}$  contours for  $V/V_{cr} = 1.15$ . None of these stresses have reached yield (50 ksi, 345 MPa), and the magnitude of  $\sigma_{min}$  (compressive principal stress) is comparable to that of  $\sigma_{max}$  (tension principal stress). At an elastic buckling load of 344 kips (1532 KN), the elastic buckling stress theoretically equals 13.7 ksi (95 MPa). At  $V = 1.15 \times V_{cr}$ , Figure 8 shows that both  $\sigma_{min}$  and  $\sigma_{max}$  have generally increased beyond 13.7 ksi.
- *Von Mises stresses:* Figure 9 plots the von Mises stress contours for  $V/V_u = 1.15$ . As would be expected, the stresses are shown to be well below yield (50 ksi).

Though the contour patterns are similar, Figures 7, 8 and 9 all show some variation in the magnitudes of plotted results between the SP:1 and SP:5 faces of the plate. More significant levels of variation are shown for the principal and von Mises stresses in Figures 8 and 9. The stress patterns on the opposing SP:1 and SP:5 faces highlight the emergence of bending moment through the thickness of the post-buckled plate in addition to in-plane stress. These moments are caused by second-order bending due to in-plane compression of the buckled plate. Each of the three half-wavelengths of this prototype's buckled shape experiences "bulging" as the top right and bottom left corners of the plate (from B to

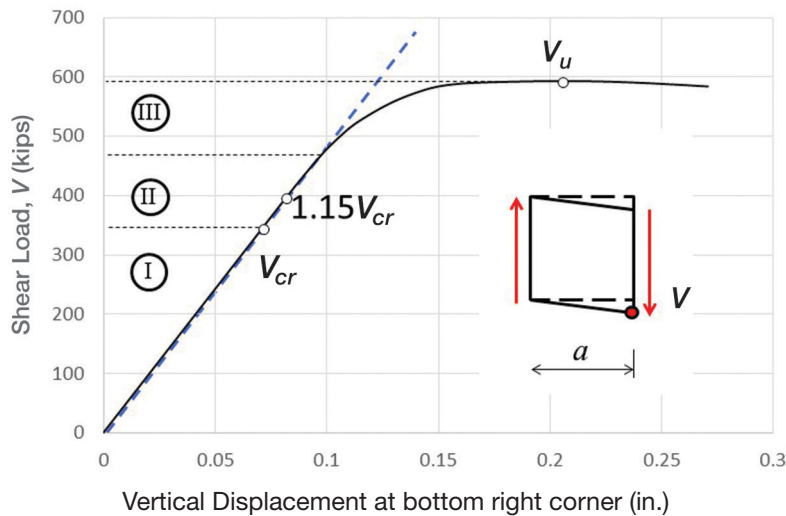


Fig. 5. Shear displacement of the plate, with  $V_{cr}$  and  $V_u$  labeled.

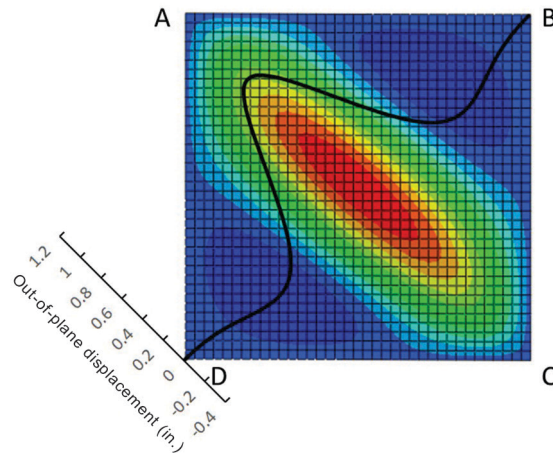


Fig. 6. Deformed shape contour at  $V_u$ , with out-of-plane deformation plot superimposed (dark black line). The face shown (front face) corresponds to SP:5; the back face (not shown) corresponds to SP:1 (see Fig. 2).

D in Figure 6) are pushed closer together by the pure shear force.

### Plate Behavior at the Ultimate Shear Post-Buckling Load, $V_u$

The following observations are made regarding the stress state of the plate when the shear,  $V$ , equals the ultimate shear post-buckling load,  $V_u = 593$  kips (2636 kN).

- *Principal stress direction,  $\theta_p$* : Figure 10 plots the  $\theta_p$  contours for  $V = V_u$ . It can be seen that this angle is no longer  $\sim 45^\circ$  and now varies between  $15^\circ$  and  $-65^\circ$ . Also, the values are now significantly different on each face (SP:1 and SP:5) because the principal stresses are also different on each face.  $\theta_p$  is shown to be largely dependent on the out-of-plane post-buckled deformation.
- *Principal stresses*: Figure 11 plots the  $\sigma_{min}$  and  $\sigma_{max}$  contours for  $V = V_u$ . Both  $\sigma_{min}$  and  $\sigma_{max}$  have reached yield in the regions marked by the bold lines encircling gray shading. The magnitudes, signs (positive, negative) and locations of these stresses are related to the out-of-plane post-buckled deformation (and bending) of the plate at  $V_u$  as seen previously in Figure 6. The  $\sigma_{max}$  contours for SP:5 in Figure 11 show a distinct band of yielding in the tension field direction, which generally supports the assumptions in the current state of practice. However, the  $\sigma_{max}$  contours for SP:1 show much lower maximum stress (actually remaining negative in compression) in

this same region due to bending. The  $\sigma_{min}$  stresses at yield are located along the tension field for SP:1 and along two smaller bands that are parallel to the tension field at SP:5. These stresses represent the compression face of bending in the buckled half-wavelength bulges along the diagonal. The emergence of these large compressive stresses on the SP:1 face indicates that the large tensile stresses in the tension field on the SP:5 face are caused by a combination of in-plane stress and second-order bending.

- *Von Mises stresses*: Figure 12 plots the von Mises stress contours for  $V = V_u$ . Nearly the entire plate surface has reached the von Mises yield condition (at 50 ksi, again shown with bold lines and gray shading) on both faces. At ultimate shear, the plate experiences a near saturation of von Mises yielding due to the combination of internal forces that develops in its buckled shape. Figure 12 shows that face SP:5 experiences a more widespread saturation of von Mises yielding than SP:1, which has a distinct band of yielding along the tension field diagonal and two other “pockets” of yield parallel to it. Note that bending-induced compression stress has caused von Mises yielding in the tension field diagonal on face SP:1 rather than in-plane tensile stresses. This deviates from the current state of practice, which assumes in-plane stress to be the primary contributor to reaching ultimate shear capacity.
- *Equivalent plastic strains*: Figure 13 plots (for  $V = V_u$ ) the equivalent plastic strains normalized by the yield

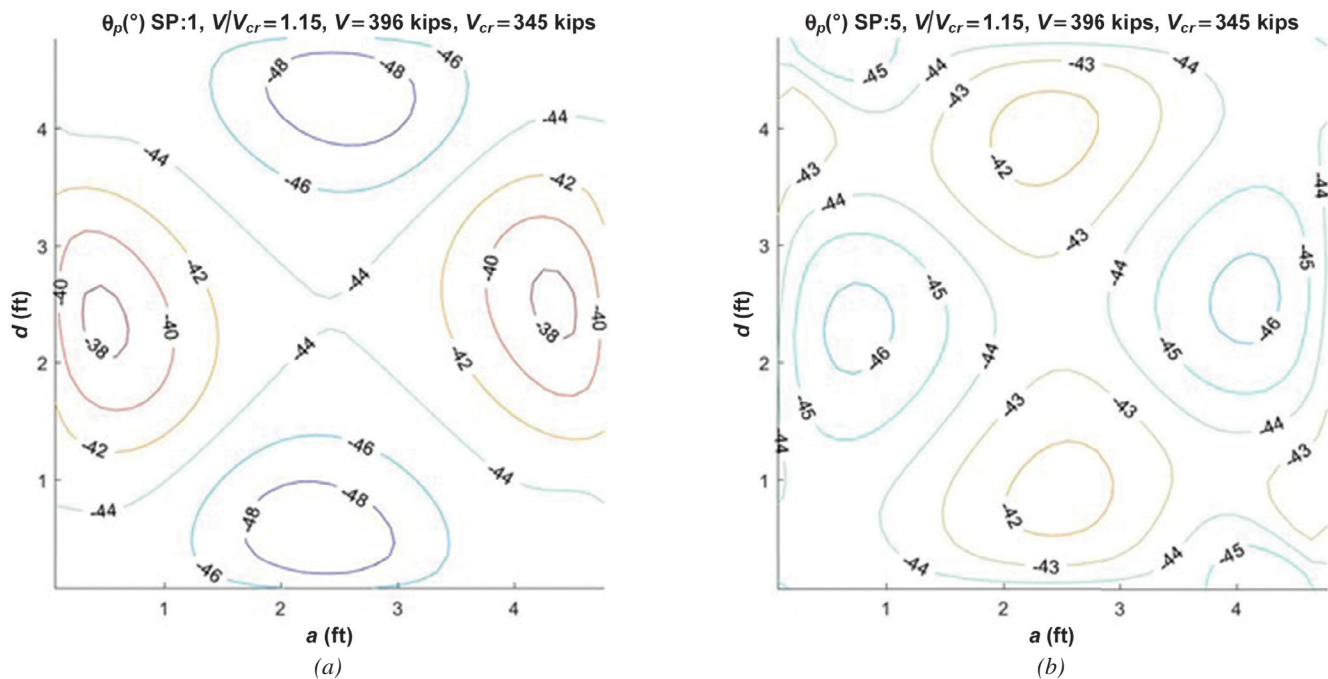


Fig. 7. Principal stress direction,  $\theta_p$ , for  $V/V_{cr} = 1.15$  in degrees: (a) = SP:1; (b) = SP:5 (see Figs. 2, 3).

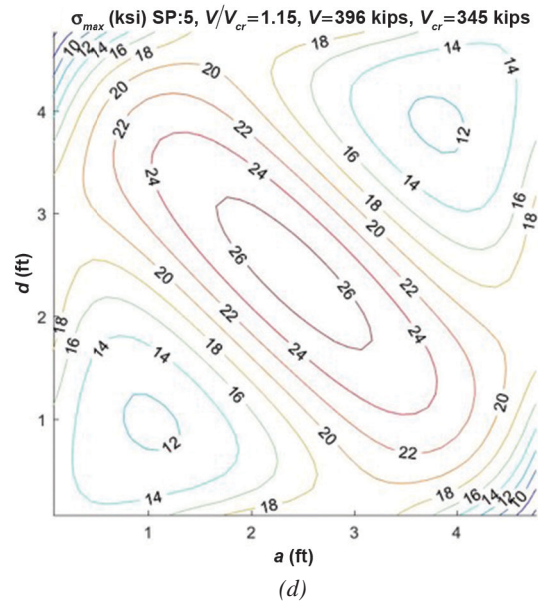
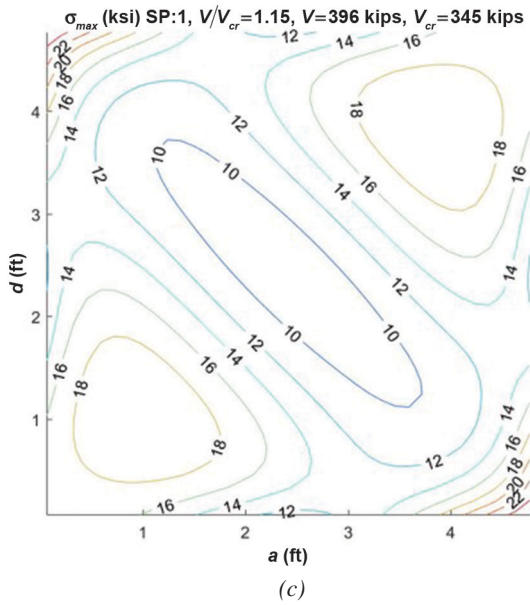
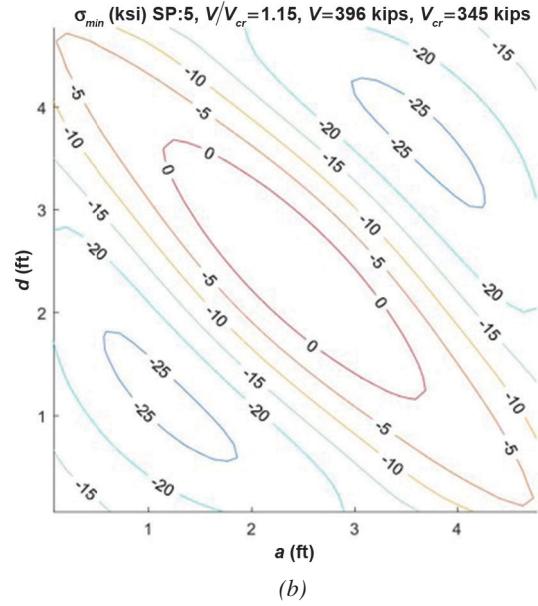
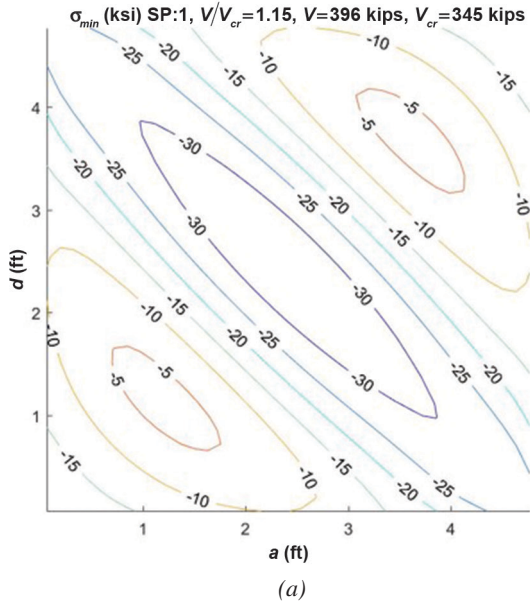


Fig. 8. Principal stresses  $\sigma_{min}$  (a; b) and  $\sigma_{max}$  (c; d) for  $V/V_{cr}=1.15$  (ksi): (a), (c) = SP:1; (b), (d) = SP:5 (see Figs. 2, 3).

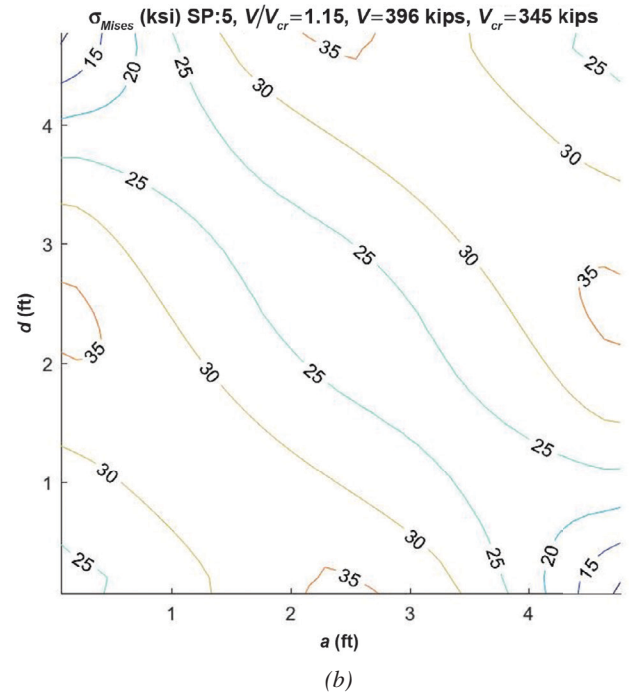
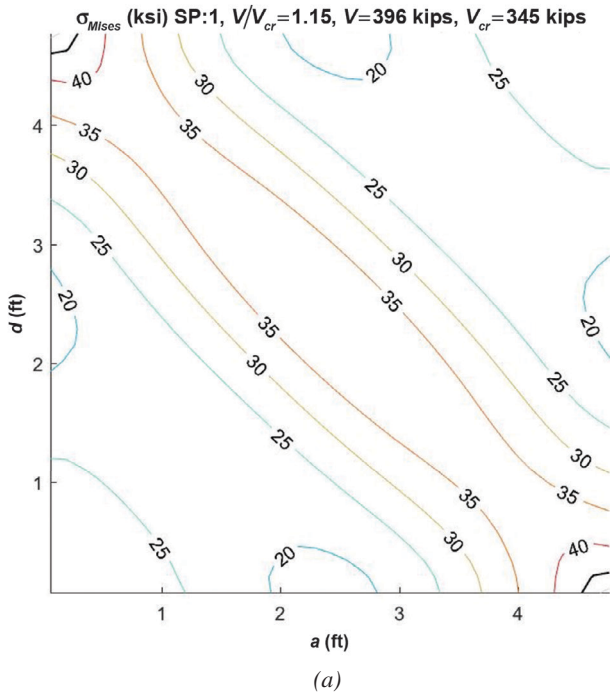


Fig. 9. Von Mises stresses for  $V/V_{cr} = 1.15$  (ksi). (a) = SP:1; (b) = SP:5 (see Figs. 2, 3, 4).

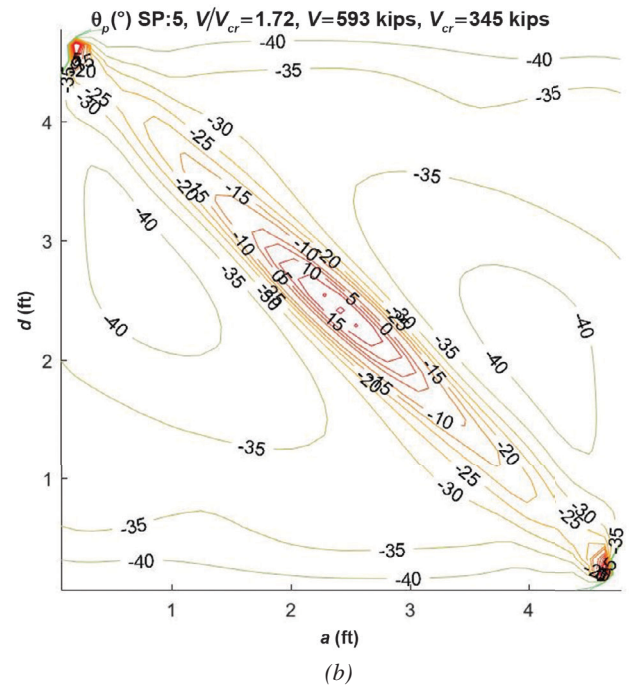
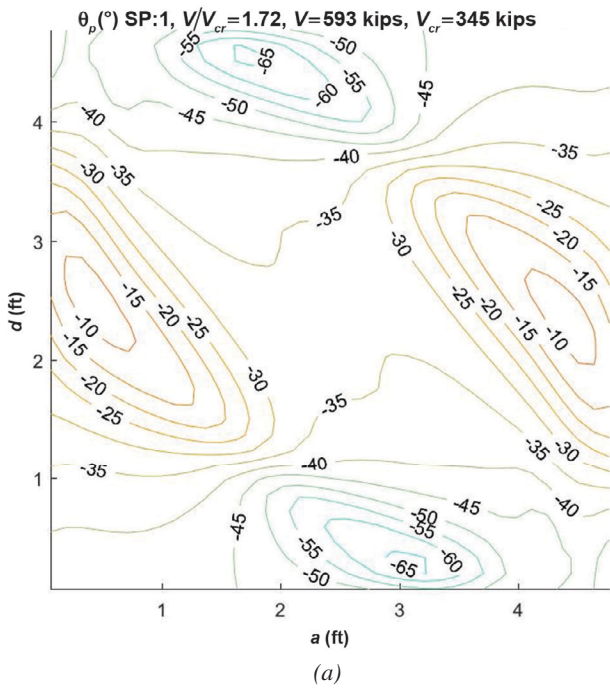


Fig. 10. Principal stress direction,  $\theta_p$ , for  $V = V_u$  in degrees: (a) = SP:1; (b) = SP:5 (see Figs. 2, 3).



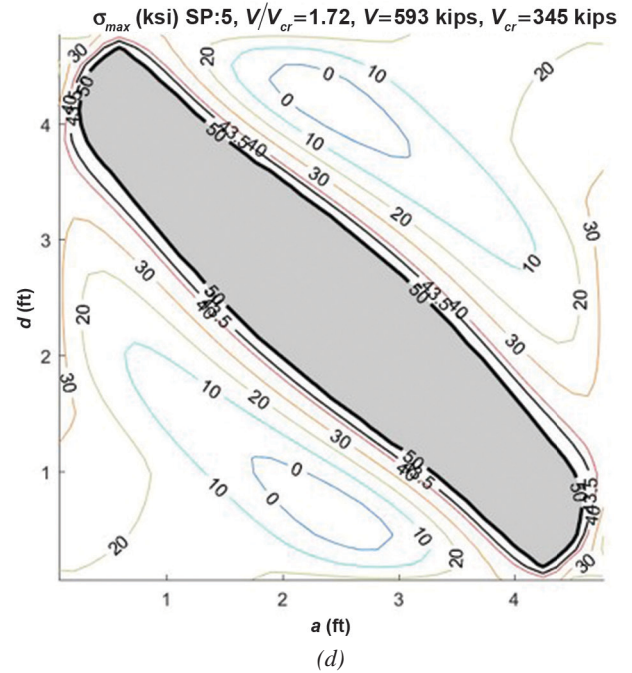
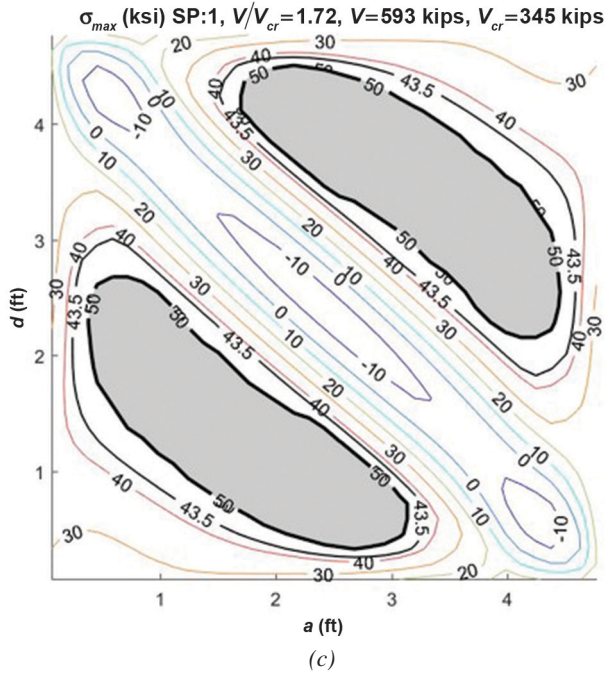
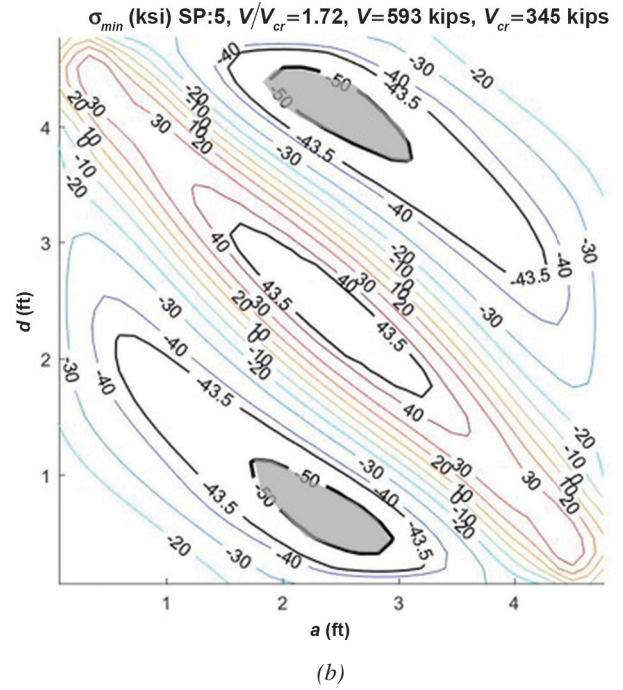
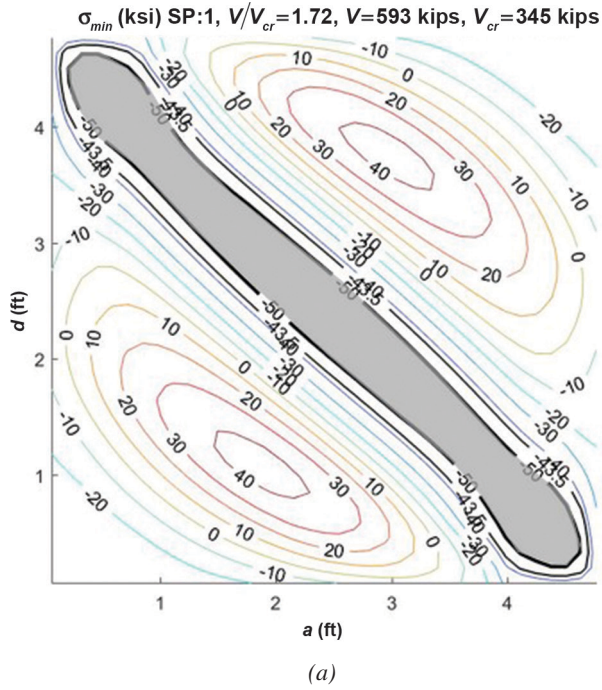


Fig. 11. Principal stresses  $\sigma_{min}$  (a; b) and  $\sigma_{max}$  (c; d) for  $V = V_u$  (ksi). (a), (c) = SP:1; (b), (d) = SP:5 (see Figs. 2, 3). Gray-shaded regions represent areas that have reached yield.

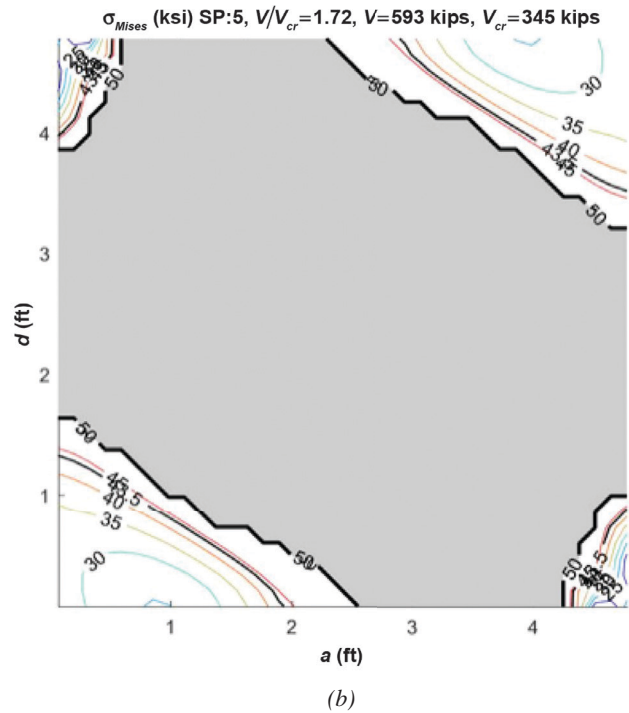
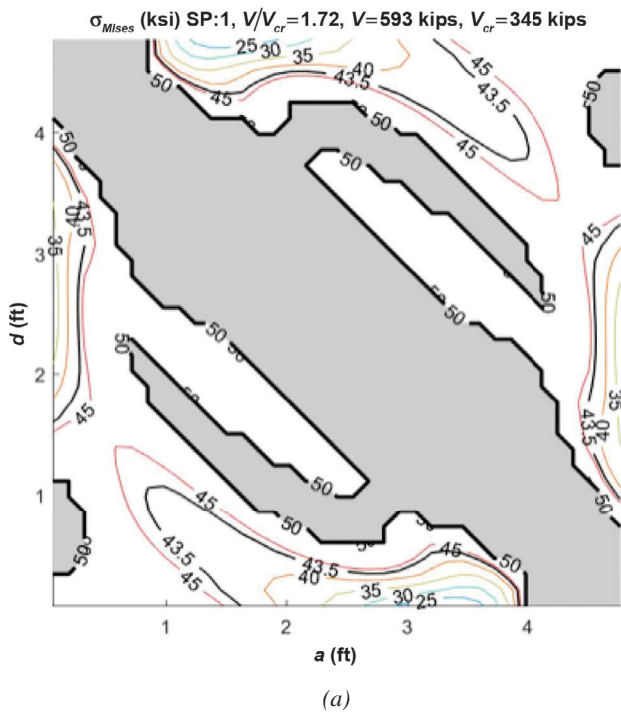


Fig. 12. Von Mises stresses for  $V = V_u$  (ksi): (a) = SP:1; (b) = SP:5 (see Figs. 2, 4). Gray-shaded regions represent areas that have reached yield.

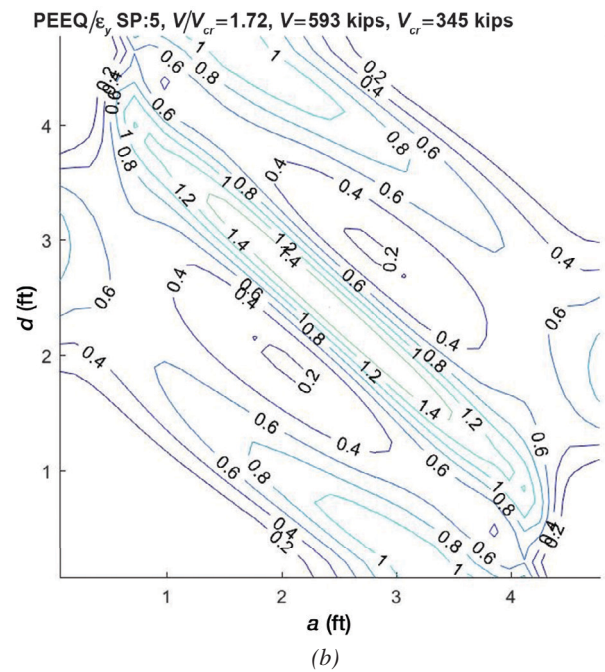
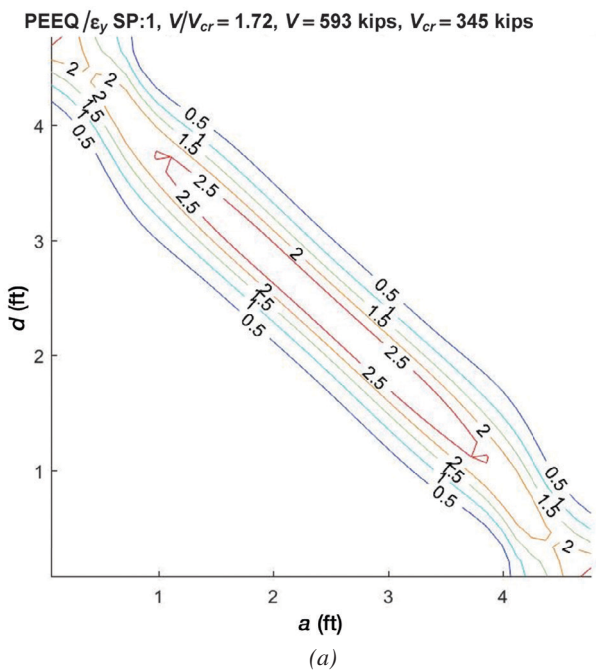


Fig. 13. Equivalent plastic strains normalized by yield strain ( $\epsilon_y = 0.001725$ ) for  $V = V_u$ : (a) = SP:1; (b) = SP:5.

strain ( $\epsilon_y = 0.001725$ ) to provide a relative measurement of ductility utilization. This value quantifies the plastic strain as related to von Mises plasticity. When comparing to Figure 12, it can be seen that these strain values are greater than zero only where yield has been reached. In the tension field region, the equivalent plastic strains are larger than  $2 \times \epsilon_y$  on one face and just slightly greater than  $\epsilon_y$  on the other face. The material model assumes strain hardening begins at a strain value equal to 0.02. From Figure 12, it can be inferred that the strains in the plates are well below this value.

### Bending Stresses at the Ultimate Shear Post-Buckling Load, $V_u$

The results presented thus far indicate that bending through the thickness of the plate due to post-buckled out-of-plane deformations has a large effect on the stress distribution. In this section, the axial stress is distinguished from the bending stress for both  $\sigma_1$  and  $\sigma_2$  (see Figure 3). The stresses are output at the five section points (SPs; i.e., the through-thickness integration points) through the shell element thickness (see Figure 2). Abaqus outputs the total stress and the average section stress (i.e., membrane axial stress) at each SP. The bending stress is calculated by subtracting the membrane stress from the total stress.

Figure 14 presents the axial (in-plane) and bending (second-order) stresses through the plate thickness for  $V = V_u$  (ksi). Figure 14(a) represents stress patterns typically seen along the tension field. These stresses are nearly linear through the depth and become slightly nonlinear at the top and bottom surface, where the stresses, considering von Mises plasticity, have reached yield. Figure 14(b) represents stress patterns typically seen outside of the tension field (near-upper-right and lower-left corners). In these regions,

the stresses are linear through the depth and smaller than those in the tension field.

Figure 15 presents the axial stress (top row) and bending stress at SP:1 and SP:5 (middle and lower rows) for both  $\sigma_1$  (left column) and  $\sigma_2$  (right column). It is clearly seen that bending stresses dominate because their magnitudes are nearly two times larger than axial stress for  $\sigma_1$  and on the order of 10 times larger for  $\sigma_2$ . These plots clearly show that second-order moment in the post-buckled shape makes a significant contribution to the onset of ultimate shear capacity.

Figure 16 provides additional illustration of the bending in the plate by plotting  $\sigma_{min}$  and  $\sigma_{max}$  at the shell element in the center of the plate against the vertical plate displacement at the bottom corner for both SP:1 and SP:5. The point of elastic shear buckling when  $V_{cr}$  is reached is clearly shown where SP:1 and SP:5 bifurcate for both  $\sigma_{min}$  and  $\sigma_{max}$ . This increasing divergence clearly indicates the onset of second-order bending moment through the thickness of the plate. At  $V_u$ , SP:1 and SP:5 are significantly different for both  $\sigma_{min}$  and  $\sigma_{max}$ .

### Membrane Stresses at the Ultimate Shear Post-Buckling Load, $V_u$

It is worthwhile to observe the influence of stresses independent of bending effects. Thus, this section discusses the membrane stresses (i.e., the axial stresses), which are equal to the membrane forces divided by the plate thickness. Figure 17 plots the membrane stresses along the diagonal directions of the compression and tension paths (at  $-45^\circ$  and  $+45^\circ$ , respectively) when the shear load equals  $V_u$ . Figure 17(a) marks with a thick bold line the 13.7-ksi (95-MPa) contour, which represents the stress at the elastic shear buckling load,  $V_{cr}$ . Inside the dark bold line, stresses are at or below 13.7 ksi, while outside of this region compressive stresses

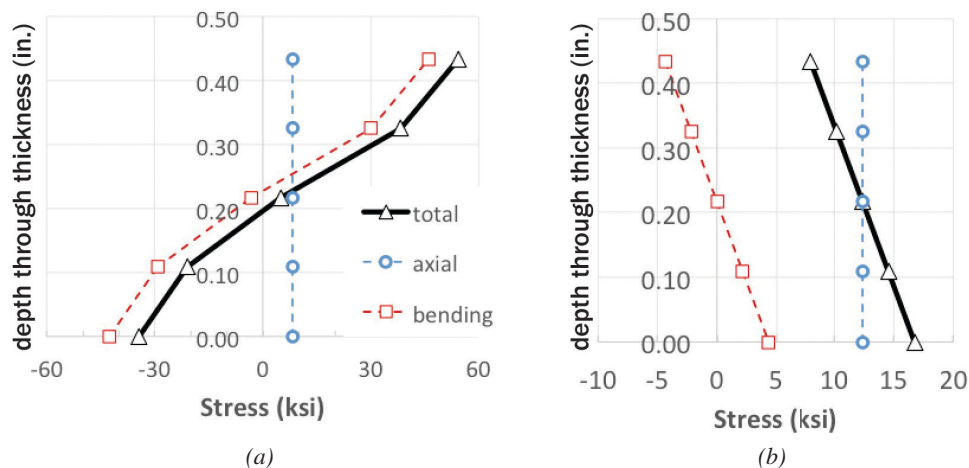
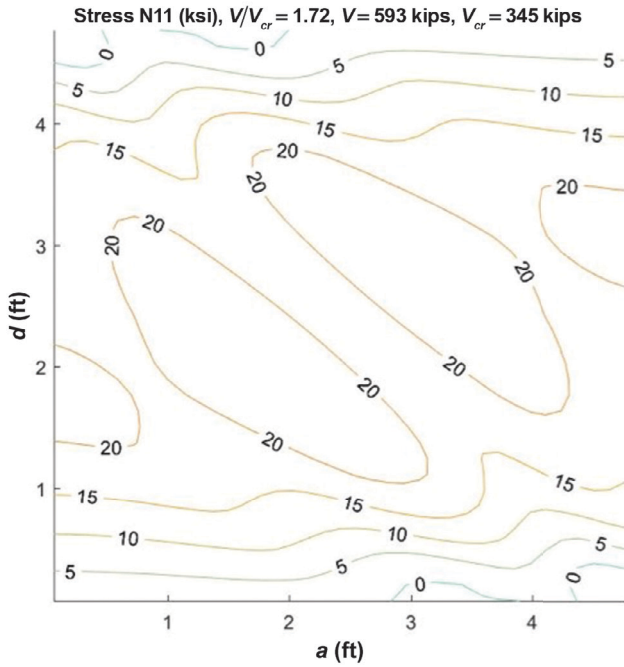
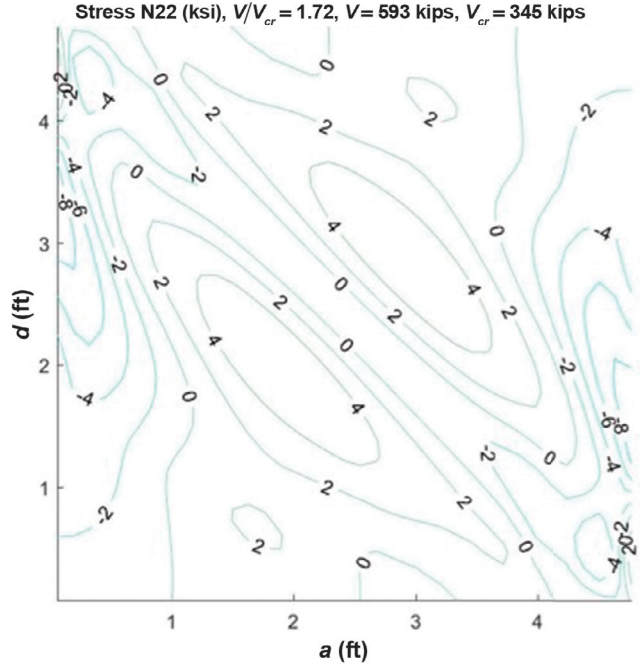


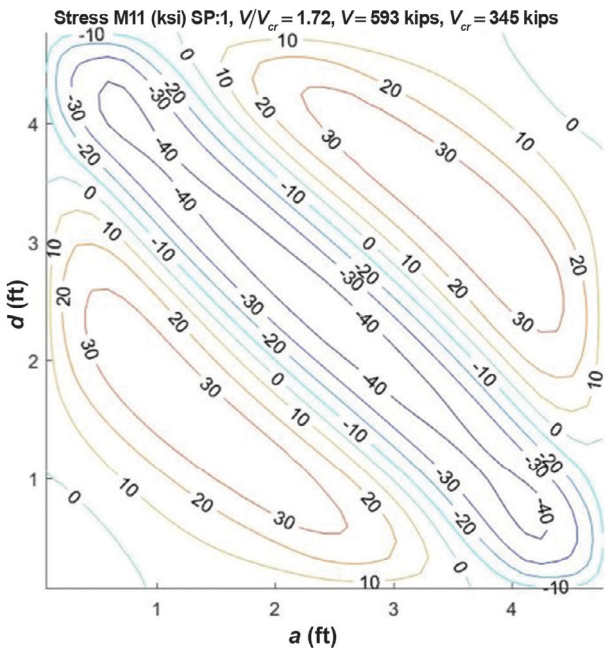
Fig. 14. Plot of axial and bending stresses in the  $\sigma_1$  direction through the plate thickness for  $V = V_u$ : (a) representative stresses along tension field; (b) = representative stresses outside of tension field (near-upper-right and lower-left corners).



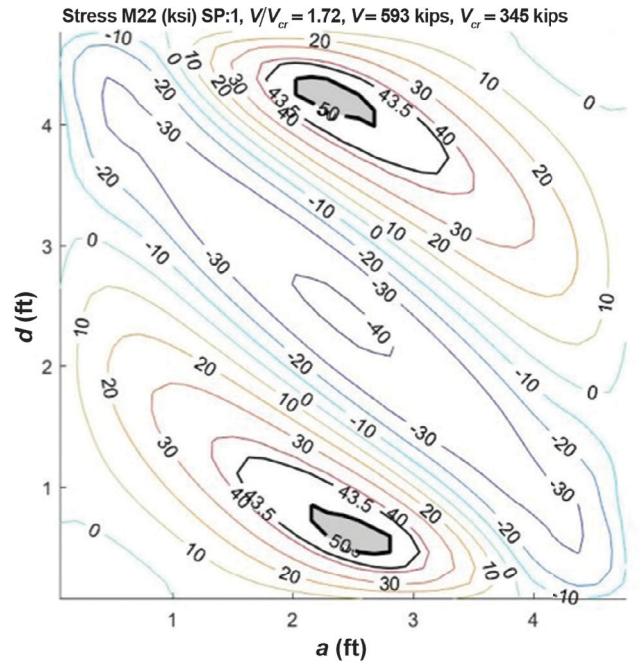
(a) Axial stress—for  $\sigma_1$  direction



(b) Axial stress—for  $\sigma_2$  direction

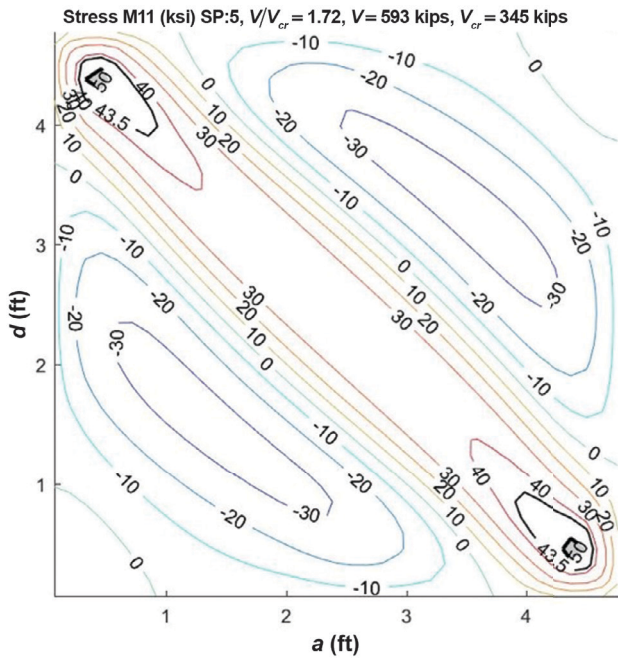


(c) Bending stress—for  $\sigma_1$  direction; SP:1 face

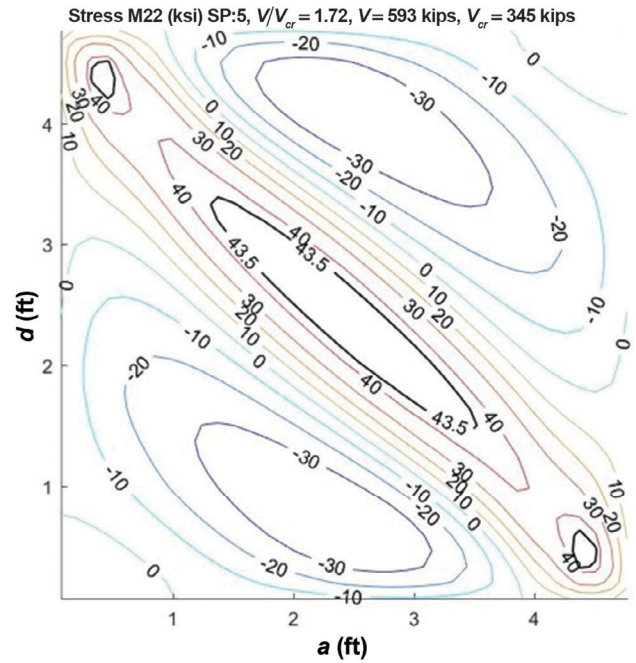


(d) Bending stress—for  $\sigma_2$  direction; SP:1 face

Fig. 15(a-d). Axial and bending stresses for  $V = V_u$  (ksi). Left figures are for  $\sigma_1$  and right are for  $\sigma_2$ .



(e) Bending stress—for  $\sigma_1$  direction; SP:5 face



(f) Bending stress—for  $\sigma_2$  direction; SP:5 face

Fig. 15(e-f). Axial and bending stresses for  $V = V_u$  (ksi). Left figures are for  $\sigma_1$  and right are for  $\sigma_2$ .

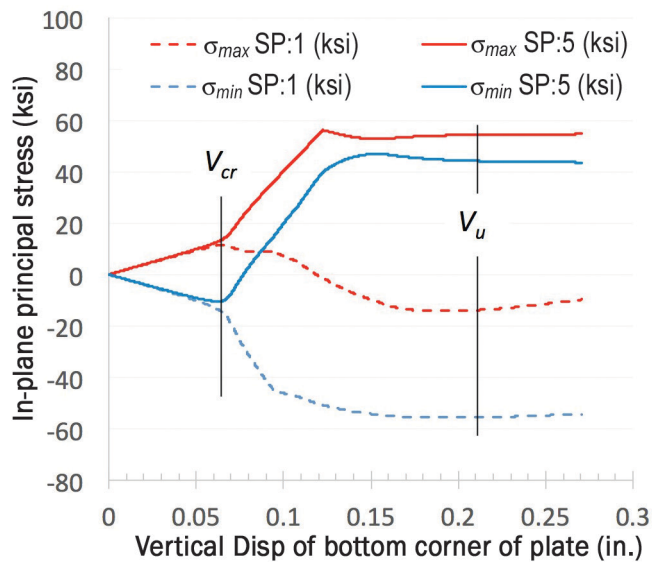


Fig. 16.  $\sigma_{min}$  and  $\sigma_{max}$  for the shell element in the center of the plate on both surfaces SP:1 and SP:5. Elastic shear buckling,  $V_{cr}$ , and ultimate shear post-buckling,  $V_u$ , are labeled.

reach up to 26 ksi. This figure illustrates that compression continues to grow beyond  $V_{cr}$ , which is contrary to tension field theory assumption. Yoo and Lee (2006) have similarly shown that compression stresses will increase beyond elastic buckling, predominantly along the edges of the web panel. Figure 17(b) shows that tension stresses range from 24 to 40 ksi; the tension field has a stiffer load path as illustrated in the conceptual sketches in Figure 17, which translates into larger stresses.

Figure 18 plots the diagonal membrane stresses versus shear load for every element along the corner-to-corner diagonal of the tension path [Figure 18(a)] and compression path [Figure 18(b)]. One curve is plotted for each element, and because the results are perfectly symmetrical, it appears

as though only half the elements on each diagonal are plotted. The orange curves represent the elements that are inside of the bold black contour of Figure 17(a)—that is, with compressive stresses equal to or less than 13.7 ksi at  $V_u$ . Green lines represent the elements that fall outside of this region. Figure 18(a) shows that all of the elements in the tension diagonal continue to increase beyond the 13.7 ksi reached at  $V_{cr}$ .

Figure 18(b) shows that after elastic buckling, compressive stresses continue to increase for all elements along the compression diagonal. An overall reduction in the rate of stress increase is observed after elastic buckling, with elements inside of the 13.7-ksi ring experiencing a larger reduction than elements outside of the ring. While Figure 17(a)

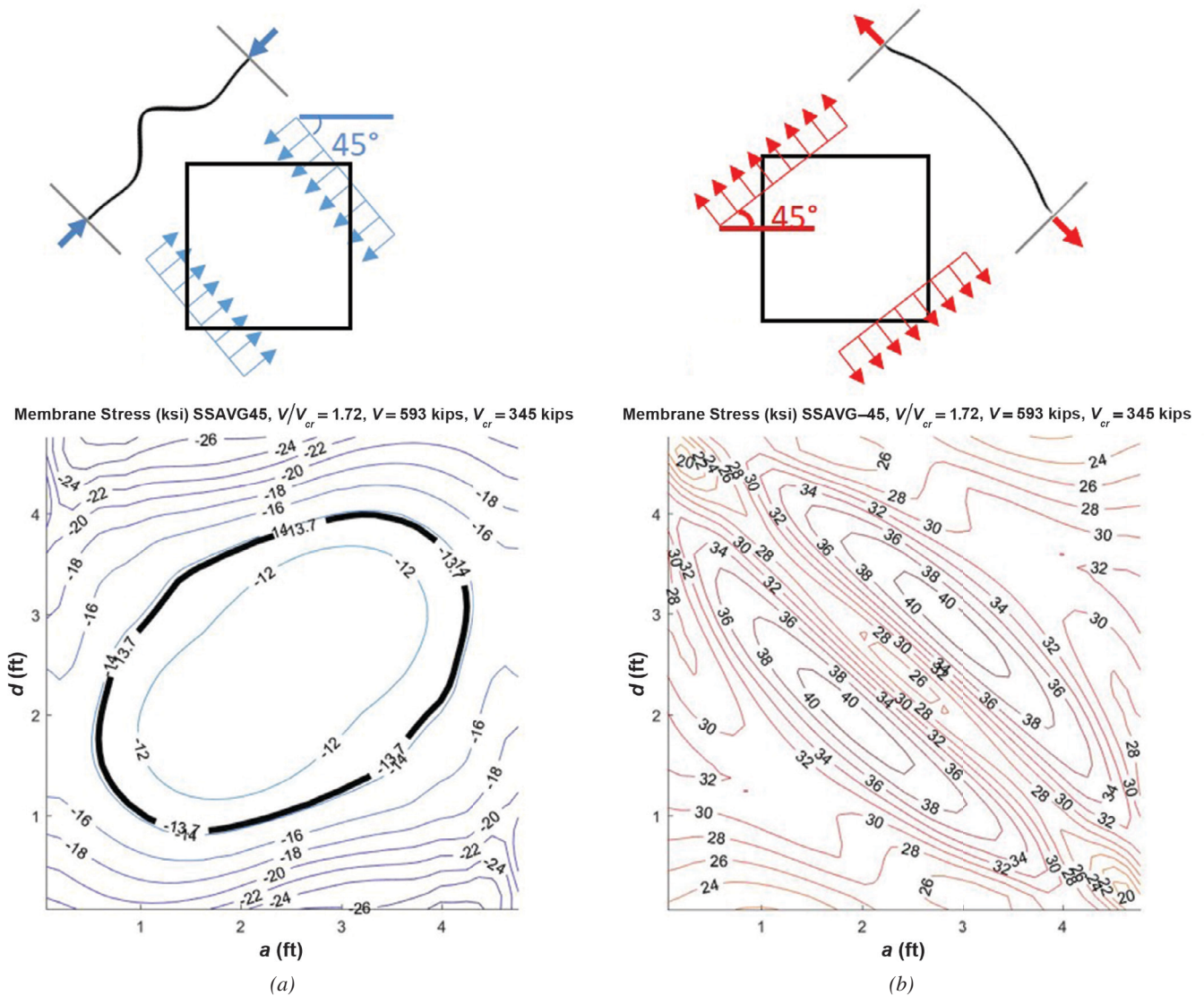


Fig. 17. (a) Compressive and (b) tensile membrane stresses (ksi) at  $V_u$  acting along the 45° diagonal directions shown.

shows that at  $V_u$ , some compressive stresses are below 13.7 ksi ( $\sigma_{min}$  at  $V_{cr}$ ), Figure 18(b) shows that these elements reached stresses larger than 13.7 ksi before decreasing prior to failure.

The “intermediate” shear load  $V_i$  marked in Figure 18(b) represents the point at which an element along the compression diagonal first experiences a stress decrease. Note how  $V_i$  correlates to the transition from phase II to phase III in Figure 5. A change in stiffness in the load-deformation behavior occurs when the compression diagonal elements near the center of the plate experience reduced membrane stresses. The additional load-carrying capacity of a plate beyond  $V_{cr}$  is equal to  $V_u - V_{cr}$  (see Figure 5). Figures 5 and 18 together show that about half of that additional capacity occurs while the compression load path is still in place and compressive stresses are increasing throughout. Compression is thus playing a clear role in developing the post-buckling shear strength.

The membrane stresses along the diagonal directions of the compression and tension paths (at  $-45^\circ$  and  $+45^\circ$ , respectively) at  $V_i$  are shown in Figure 19. It is observed that the compressive stresses in all elements do indeed exceed that at  $V_{cr}$  (13.7 ksi). In the center of the plate, the tensile membrane stresses are larger than the compressive membrane stresses (24 ksi vs. 15.5 ksi, respectively), but at the edges of the web panel, they are similar.

### INTERRUPTING THE COMPRESSION PATH

The results presented in the preceding section indicate that compression and second-order bending stresses (due to large, out-of-plane deformations) play an important role in the post-buckling performance of this slender plate. While it is not clear yet how the compression behavior directly contributes to  $V_u$ , studies that interrupt the compression field, as presented in this section, can provide some clues. To

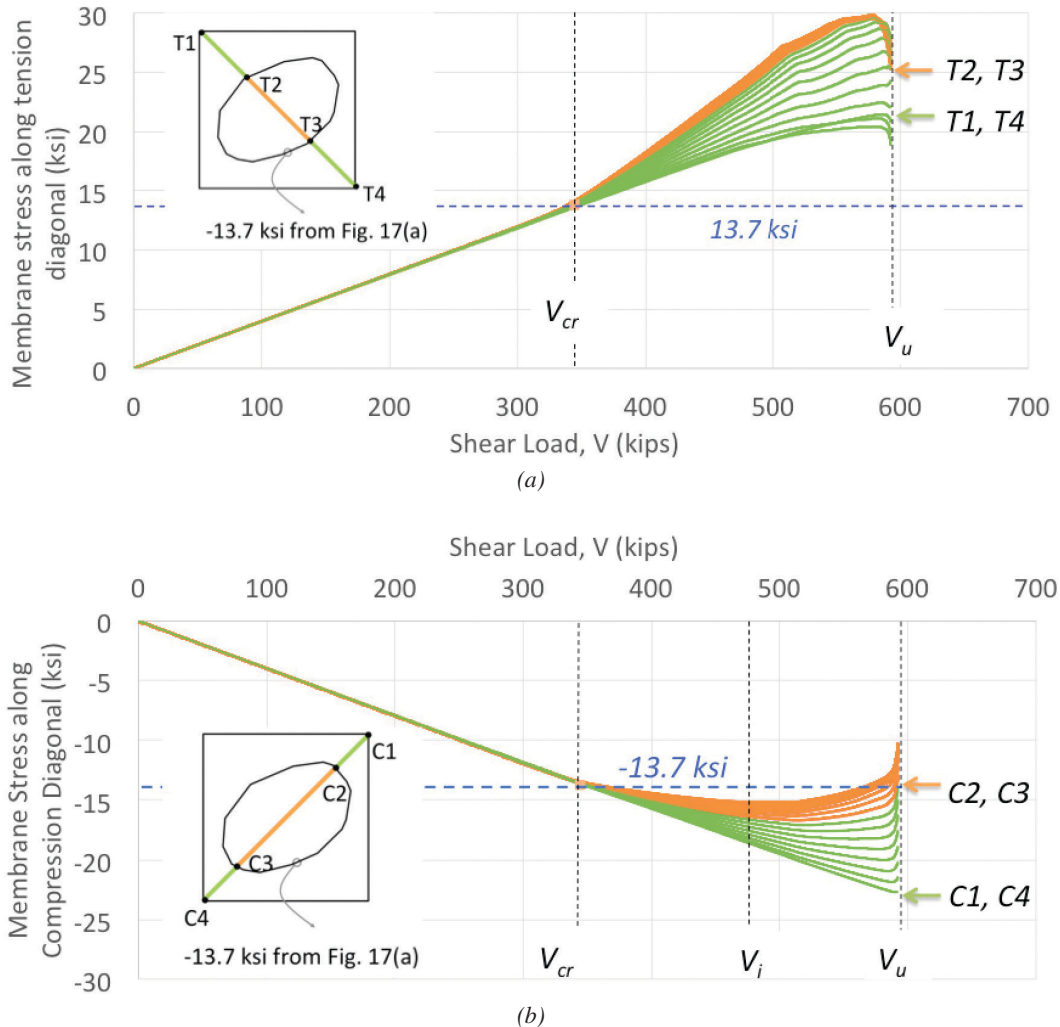


Fig. 18. Plot of membrane stresses versus applied shear load for finite elements along the (a) tension diagonal and (b) compression diagonal.

this end, the plate was modified in two ways: (1) by cutting the compression field corners by 16% of the depth,  $D$  (model name = CUT), thus reducing the area by 3%, and (2) by cutting slits near the corners along the compression field (model name = SLITS), thus reducing the area by 1%. Images of these models and the resulting  $V_{cr}$  and  $V_u$  values obtained from finite element analysis are shown in Table 1. Contour plots of the von Mises stress when the plate reaches  $V_u$  are shown for each case in Figure 20. Contour plots of the equivalent plastic strains at  $V_u$  are shown for each case in Figure 21.

Table 1 shows that interrupting the compression field delays the onset of elastic buckling and increases  $V_{cr}$  up to 24%. For the cut case,  $V_u$  is unaffected because the cut corners do not deter the development of von Mises stress

patterns similar to the full original plate, as shown in Figure 20. For the slits case, the slits alter the von Mises stress patterns on the top face of the plate (by interrupting the edges of the von Mises stress saturation), thus reducing the ultimate shear capacity below the full plate model (a 5% reduction).

The plots of equivalent plastic strains in Figure 21 show similar patterns to the von Mises stress patterns. On the SP:1 face, these strains exceed zero only in the tension field, and all three plates show similar strain patterns despite their modifications. Furthermore, the magnitude of strain values is similar for all three plates. Although not shown, bending stresses again dominate over membrane axial stresses for the cut and slits cases as discussed previously for the full case (described in detail in Figure 15).

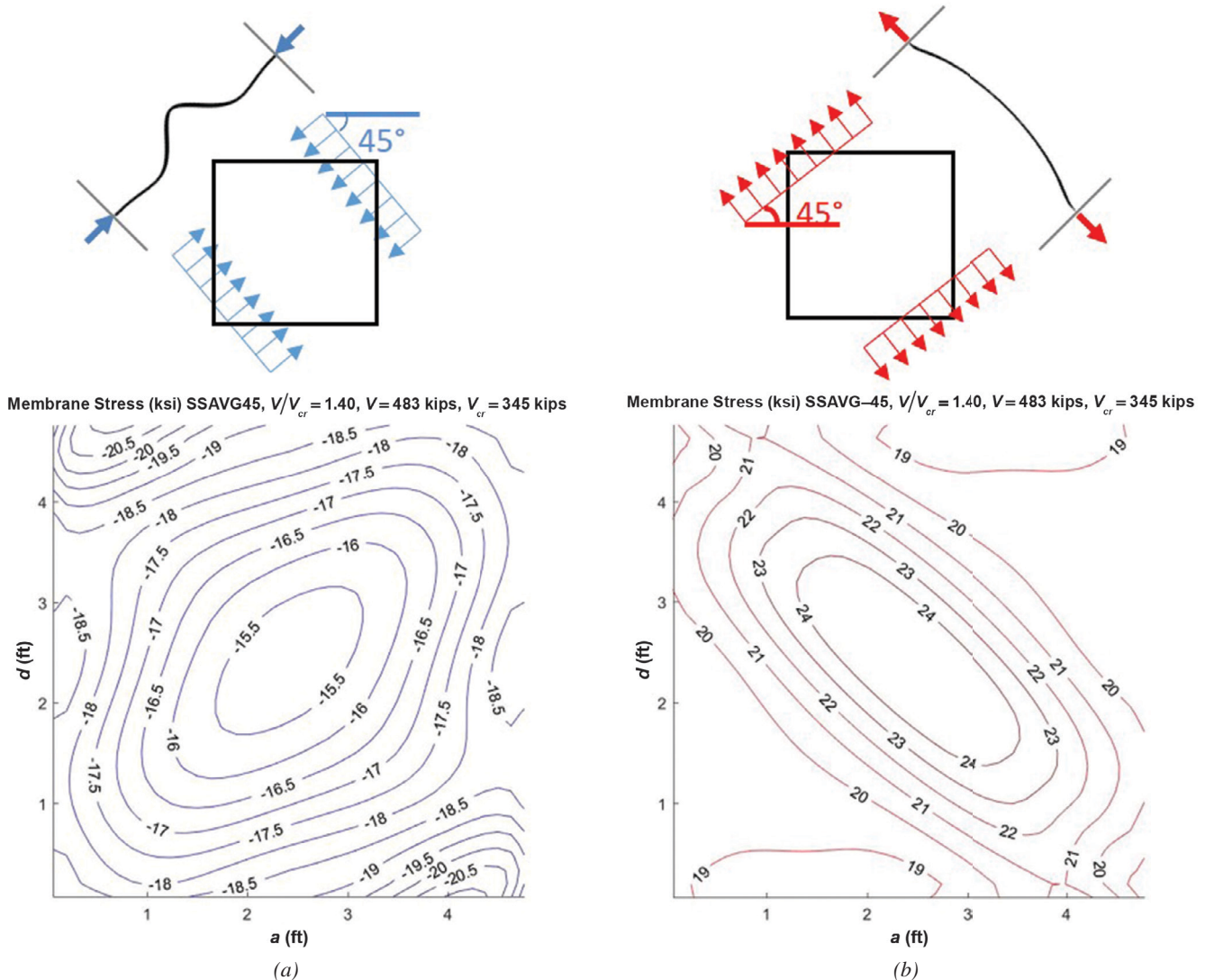

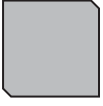
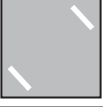


Fig. 19. (a) Compressive and (b) tensile membrane stresses (ksi) at the intermediate shear load  $V_i$  [see Fig. 18(b)], acting along the 45° diagonal directions shown.



Table 1. Finite Element Results of Modified Plates			
		$V_{cr}$ (kips)	$V_u$ (kips)
		(ratio to baseline)	
Full (baseline)		344 (1.00)	593 (1.00)
Cut		428 (1.24)	594 (1.00)
Slits		380 (1.10)	564 (0.95)

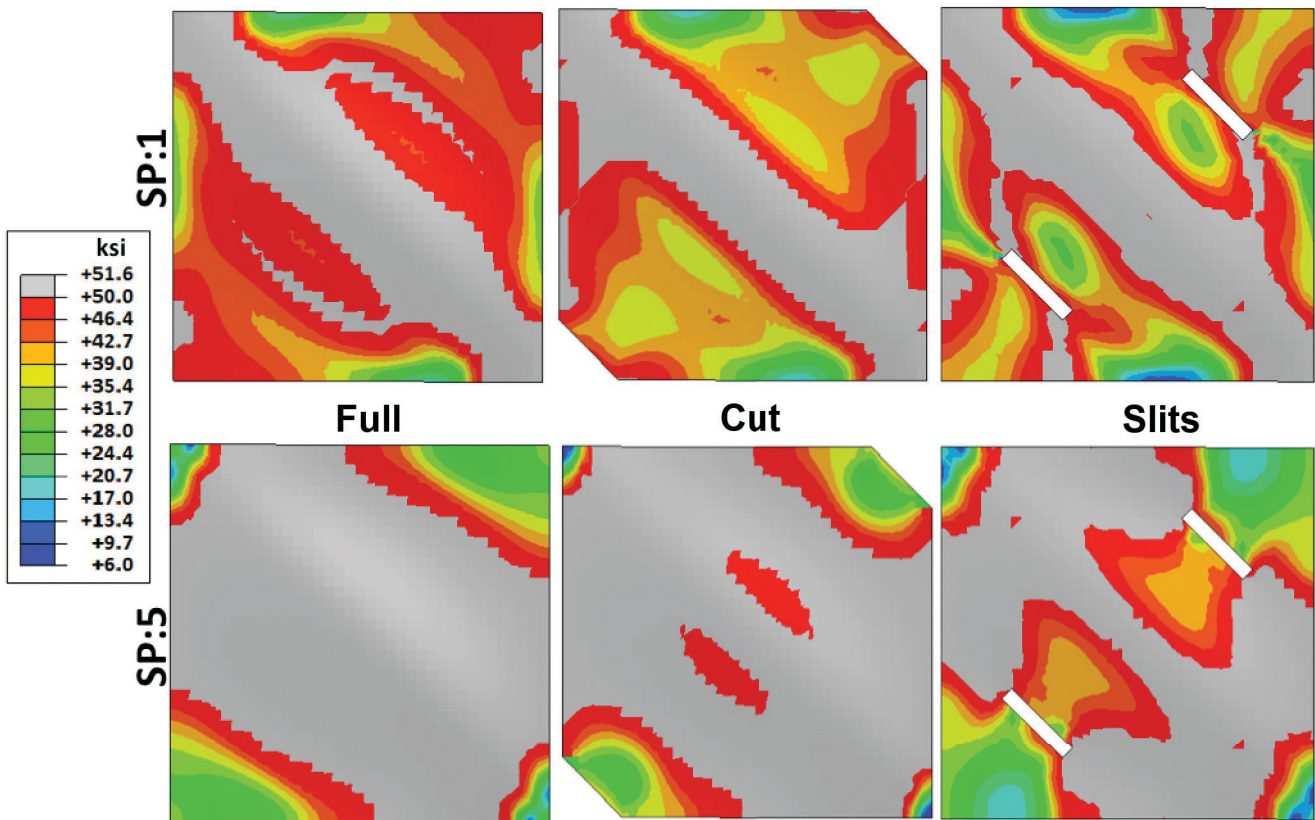


Fig. 20. Von Mises stresses at  $V = V_u$  for the full plate, the cut plate, and the plate with slits (units = ksi).

These results suggest that the elastic buckling load could be strategically modified to meet a given design objective with relatively minor modifications to the plate. The ultimate shear post-buckling load, however, is not significantly affected by these modifications. Based on these results, the authors are now exploring new potential models of ultimate plate post-buckling mechanics for thin plates that incorporate second-order bending of the post-buckled shape. Also, the mechanical impact and construction/life-cycle implications of the plate modifications will be examined in future research by the authors.

### SUMMARY AND CONCLUSIONS

Post-buckling behavior of slender webs in steel plate girders has been a mainstay of plate girder design for several decades on the basis of semi-empirical equations that were originally developed in the 1960s. Though the existing state of practice is generally conservative, the assumption of pure in-plane stress in response to shear loads after the web has buckled does not capture the full mechanical responses of the thin plate. New research by the authors has begun to reexamine the post-buckling behavior of thin steel plates by

considering the combined effects of in-plane stress and out-of-plane (second-order) bending. This study utilized a previously validated finite element modeling approach in Abaqus to analyze a prototype simply supported plate with an aspect ratio equal to 1.0. The results of these analyses showed that out-of-plane bulging of the post-buckled plate produces second-order bending moments due to compression along the diagonal opposite the tension field.

Although the conclusions summarized here are based only on the plate dimensions of this initial study, these results point to future research that is needed. The results are also relevant to plates of other proportions that demonstrate shear post-buckling behavior that is physically characterized by significant bulging/wrinkling on the diagonal (thus generating potentially significant bending stresses through the thickness).

- At the ultimate shear post-buckling load,  $V_u$ , the angle of principal stress direction is no longer  $45^\circ$  and instead varies between  $15^\circ$  (counterclockwise) and  $65^\circ$  (clockwise).
- The stress distribution through the plate thickness was separated into pure planar (i.e., axial) and bending (second-order) stresses. Bending stresses were found

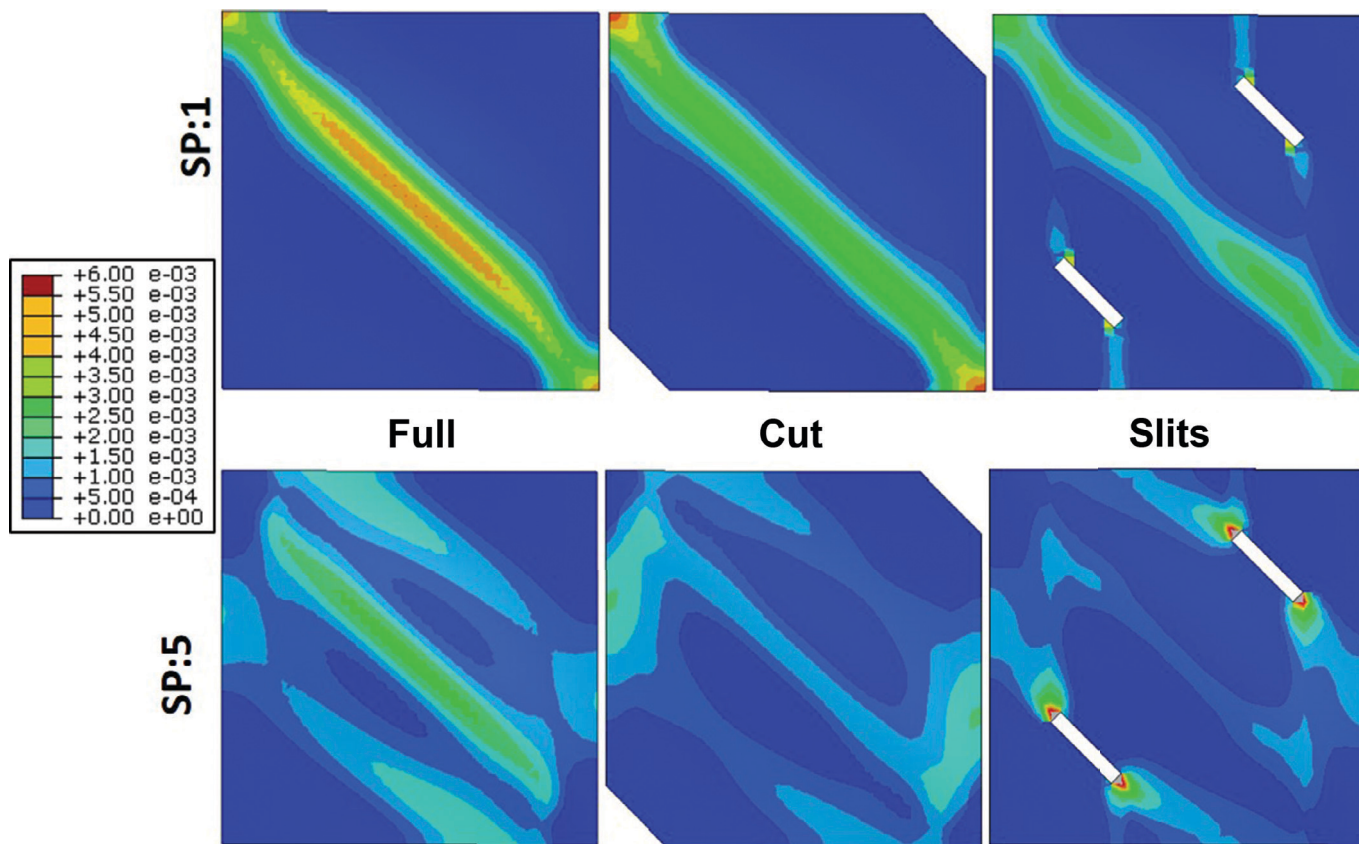


Fig. 21. Equivalent plastic strains at  $V = V_u$  for the full plate, the cut plate, and the plate with slits.

to be significantly higher than the pure planar stresses at the ultimate post-buckling shear load. These stresses are created by second-order compression of the plate's buckled shape (i.e., the buckled half-wavelengths that bulge out-of-plane along the length of the compression field diagonal).

- At the ultimate post-buckling shear load, almost the entire plate has reached the von Mises yield boundary due to a combination of planar and bending stresses. The contours of von Mises yielding show some differences, however, for the opposing faces of the plate.
- Compression membrane stresses (which are independent of the second-order bending effects) continue to increase beyond elastic buckling, contrary to the current tension field theory assumption. These results suggest that compression effects can play a significant role in the post-buckling shear response.

Building from these results, and with the intent to further investigate the plate behavior, the authors examined some simple modifications of the plate that interrupted the compression diagonal. The results of two cases, with small through-plate cuts removed from the compression diagonal, showed (1) an increase of 10% to 24% in the shear load needed to induce buckling (i.e., the elastic shear buckling load) and (2) a negligible effect on the ultimate shear post-buckling load. These results indicate that the onset of elastic buckling can be delayed by interrupting the compression field, which may prove useful for designing girder webs.

### ACKNOWLEDGMENTS

This research was sponsored by the National Science Foundation (NSF) under grants CMMI-1662886 and CMMI-1662964. Mr. Alós-Moya's involvement in this project as a Visiting Student Research Scholar at Princeton University was financially supported by the Spanish Ministry of Science and Innovation (research project BIA 2011–27104) and the Universitat Politècnica de València (Research and Development Support Program PAID-06-11). All opinions expressed in this paper are the authors' and do not necessarily reflect the policies and views of the sponsors.

### REFERENCES

AISC (2016), *Specification for Structural Steel Buildings*, ANSI/AISC 360-16, American Institute of Steel Construction, Chicago, IL.

Basler, K. (1961), "Strength of Plate Girders in Shear," *Transactions ASCE*, Vol. 128, No. 2.

Basler, K., Yen, B.T. and Mueller, J.A. (1960), "Web Buckling Tests on Welded Plate Girders," *Welding Research Council, Bulletin No. 64*, September, New York, NY.

Bergfelt, A. and Hovik, J. (1968), "Thin-Walled Deep Plate Girders under Static Loads," *Proceedings of the IABSE Colloquium*, New York, NY.

Dassault Systemes (2011), "Abaqus 6.11ef Online Documentation" [online; accessed 2017].

Evans, H.R., Rockey, K.C. and Porter, D.M. (1977), "Tests on Longitudinally Reinforced Plate Girders Subjected to Shear," *Proceedings of Conference on Structural Stability*, Liege, Belgium.

FHWA (1982), *Standard Plans for Highway Bridges*, Vol. II, "Structural Steel Superstructures," Federal Highway Administration, Washington, DC.

Glassman, J. and Garlock, M. (2016), "A Compression Model for Ultimate Postbuckling Shear Strength," *Thin-Walled Structures*, Vol. 102, pp. 258–272.

Garlock, M. and Glassman, J. (2014), "Elevated Temperature Evaluation of an Existing Analytical Model for Steel Web Shear Buckling," *Journal of Constructional Steel Research*, Vol. 101, pp. 395–406. doi:10.1016/j.jcsr.2014.05.021.

Höglund, T. (1997), "Shear Buckling Resistance of Steel and Aluminum Plate Girders," *Thin-Walled Structures*, Vol. 29, pp. 13–30.

Jha, A. (2016), "Investigation of the Shear-Strength of Built-Up I-Section Members via Test Simulation," Master's Thesis, Department of Civil and Environmental Engineering, Georgia Institute of Technology, Atlanta, GA.

Kamtekar, A.G., Dwight, J.B. and Threlfall, B.D. (1972), "Tests on Hybrid Plate Girders (Report 2)," Report No. CUED/C-Struct/TR28, Cambridge University, Cambridge, UK.

Narayanan, R. and Rockey, K.C. (1981), "Ultimate Load Capacity of Plate Girders with Webs Containing Circular Cut-Outs," *Proceedings of the Institution of Civil Engineers*, Part 2, Vol. 71, pp. 845–862.

Porter, D.M., Rockey, K.C. and Evans, H.R. (1975), "The Collapse Behavior of Plate Girders Loaded in Shear," *Structural Engineering*, Vol. 53, No. 8, pp. 313–325.

Rockey, K.C. and Skaloud, M. (1972), "The Ultimate Load Behaviour of Plate Girders Loaded in Shear," *Structural Engineer*, Vol. 50, No. 1, pp. 29–48.

Timoshenko, S.P. and Gere, J.M. (1961), *Theory of Elastic Stability*, 2nd Ed., McGraw-Hill Book Company, New York, NY.

Wagner, H. (1931), "Flat Sheet Metal Girder with Very Thin Metal Web," Technical Notes 604, 605, 606, National Advisory Committee on Aeronautics, Washington, DC.

White D.W. and Barker M.G. (2008), "Shear Resistance of Transversely Stiffened Steel I-Girders," *Journal of Structural Engineering*, Vol. 134, No. 9, pp. 1,425–1,436.

Wilson, J.M. (1886), "On Specifications for Strength of Iron Bridges," *Transactions ASCE*, Vol. 15, Part I, pp. 401–403, 489–490.

Yoo, C.H. and Lee, S.C. (2006), "Mechanics of Web Panel Postbuckling Behavior in Shear," *Journal of Structural Engineering*, Vol. 132, No. 1, pp. 1,580–1,589.

Ziemian, R.D. (2010), *Guide to Stability Design Criteria for Metal Structures*, 6th Ed., John Wiley & Sons, Hoboken, NJ.